Supplementary Information for:

Microscale fiber photoacoustic spectroscopy for in-situ and real-time trace gas sensing

Jun Ma[1,2], Enbo Fan[1,2*], Haojie Liu[1,2*], Yi Zhang[3], Cong Mai[4], Xin Li[4], Wei Jin[5], and Bai-Ou Guan[1,2]*

[1]*Guangdong Provincial Key Laboratory of Optical Fiber Sensing and Communications, Institute of Photonics Technology, Jinan University, Guangzhou 510632, China*

[2]*College of Physics &Optoelectronic Engineering, Jinan University, Guangzhou 510632, China*

[3]*College of Life Science and Technology, Jinan University, Guangzhou 510632, China*

[4]*Department of Critical Care Medicine, Guangdong Provincial People's Hospital (Guangdong Academy of Medical Sciences), Southern Medical University, Guangzhou 510080, China*

[5]*Department of Electrical and Electronic Engineering, The Hong Kong Polytechnic University, Hong Kong SAR, China*

[*]*These authors contribute equally to this work.*

Corresponding authors: wei.jin@polyu.edu.hk (W. Jin); tguanbo@jnu.edu.cn (B.-O. Guan)

Supplementary Note 1. Membrane preparation based on photothermal actuation

Fig. S1(a) shows the schematic of the photothermal fabrication process of the fiber photoacoustic spectrometer (FPAS) as described in the section **Methods**. During the fabrication process, once the 980 nm heating light is turned off (Step iv), the air pressure in the cavity reduces and becomes lower than that outside the cavity. Fig. S1(b) are the microscopic images of the membrane suspended in the capillary before and after turning off the heating light. The existing pressure difference pushes the pre-cured membrane inward the cavity and makes the membrane stretched. After fully curing the membrane with UV light illumination for several hours, the flat membrane with in-plane pre-stress is obtained. The reflection spectra of the FPAS with different membrane thickness are measured by an optical spectrum analyzer (OSA, Yokogawa, AQ6370B) and a broadband amplified spontaneous emission (ASE) source (Golight, ASE-C+L), as shown in Fig. S1(c). The envelope of the interference spectrum is attributed to the multi-beam interface from the fiber tip facet and the two surfaces of the membrane. The UV-curable gel for preparing the membrane has a refractive index of ~ 1.52[62], which corresponds to an optical reflectivity of ~ 4.3 % based on the Fresnel formula. The slightly larger reflectivity of the membrane than that of the fiber endfacet (~ 3.4%) can compensate part of the transmission loss of the light travelling forth and back through the cavity, which can benefit a large fringe contrast of over 20 dB for the reflection spectrum as shown in Fig. S1(c) and thus increase the acoustic sensitivity of the FPAS interrogated by a narrowband probe laser with the wavelength at the quadrature point of the spectrum. Based on the interference principle, the distance between the single-mode fiber (SMF) end facet and the UV glue film, i.e., the length of the Fabry-Perot (F-P) cavity, can be inferred from the fringe period of the interference spectrum while the membrane thickness can be estimated from the period of the envelope of the fringes.

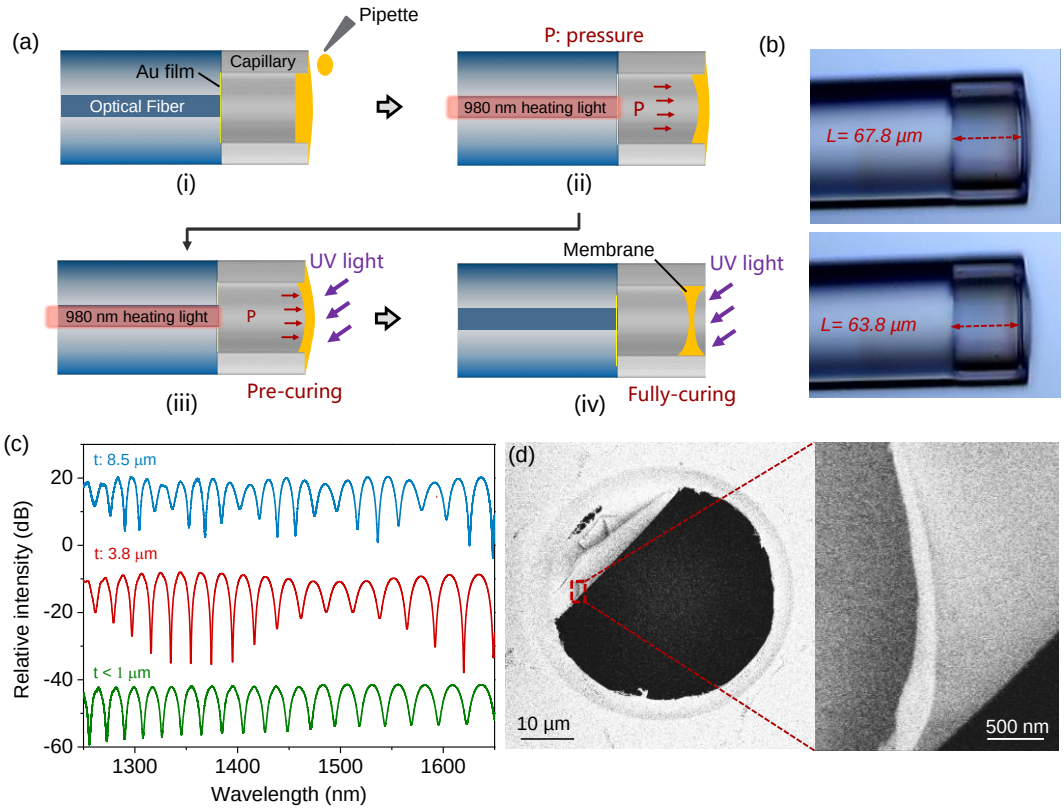

Fig. S1. (a) Schematic of the membrane preparation process based on photothermal actuation mechanism. (b) Microscopic images of the membrane suspended in the capillary before and after turning off the heating light. (c) The reflection spectrum of the FPAS with membranes of different thickness. (d) SEM image of the scratched membrane with a curling edge. P: pressure; UV: ultraviolet.

As the membrane thickness reduces, the envelope period increases. By fine tuning of the heating power and the volume of the UV adhesive droplet dipped into the capillary, the thickness of the polymer membrane after UV curing can be gradually reduced from several micrometers down to sub-micrometer. At the heating power of 20 mW, the membrane thickness is reduced to ~ 200 nm. For this submicron-thick membrane, it is nearly impossible to estimate its thickness from the interference spectrum. To measure the exact thickness, the exposed edge of a membrane scratched by the femtosecond (fs) laser is imaged by the scanning electronic microscope (SEM), as shown in Fig. S1(d).

To diminish the influence of the environmental disturbances such as the air flow, four holes with the size of several micrometers are opened evenly along the membrane edge using the fs laser following the arc-shaped inscription traces as sketched in Fig. S2(a). The SEM images of the membrane with different hole sizes processed by the fs laser are shown in Fig. S2(b).

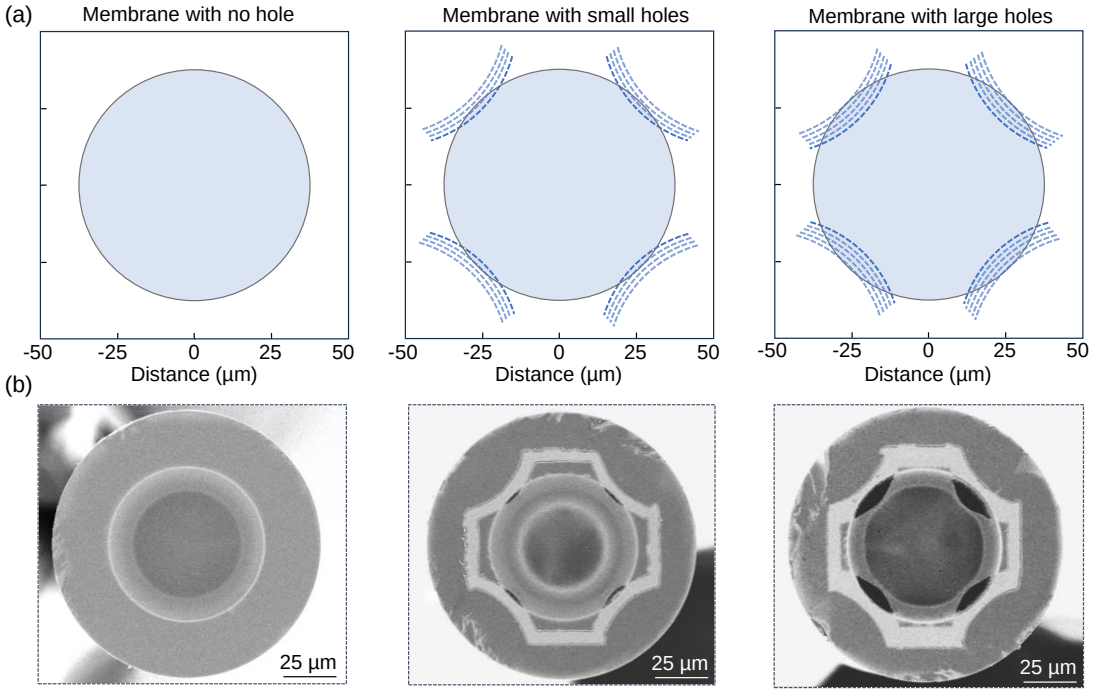

Fig. S2. (a) Schematic of the inscription trace for fs-laser patterning the holes in the membrane. The dash line denotes the traces of the laser spot during the inscription. (b) SEM image of FPAS with an intact membrane and two membranes with fs laser-pattered holes of different sizes.

Supplementary Note 2. Analysis of the FPAS acoustic response with equivalent circuit

Equivalent circuit with the lumped elements is used to analyze the acoustic characteristics of the FPAS[33,63,64]. As shown in Fig. S3, *M*, *R* and *C* in the circuit denote the electrical inductance, resistance and capacitance, respectively. For a simple sinusoidal acoustic wave at the angular frequency *w*, the corresponding acoustic impedances are then *jwM*, *R*, and *1/jwC*, respectively.

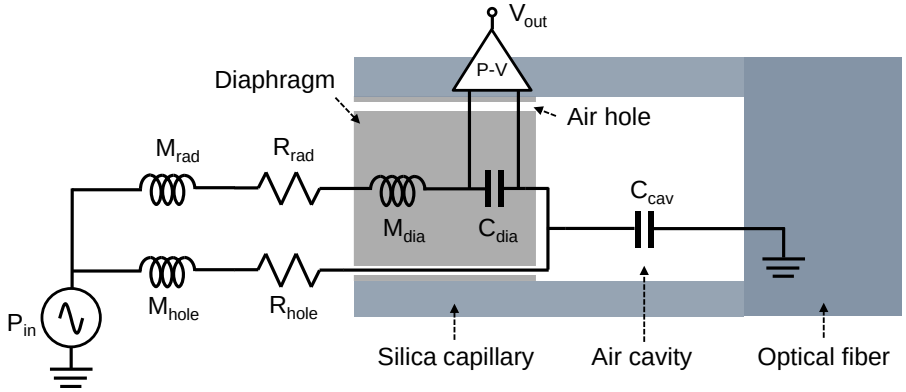

Fig. S3. Schematic of the equivalent circuit with lumped elements for analyzing the frequency response of the FPAS to acoustic waves.

The parameters for the lumped elements include the radiation mass (M_{rad}) and resistance (R_{rad}) of the diaphragm (i.e., the polymer membrane here), the acoustic mass (M_{dia}) and the compliance (C_{dia}) of the diaphragm, the acoustic mass (M_{hole}) of the holes in the diaphragm, the viscous resistance for vertical (R_{holeV}) and horizontal (R_{holeH}) air flow through the holes, and the compliance (C_{Cav}) of the air cavity, as listed in Table S1. The geometric parameters of the diaphragm and cavity as well as the physical constants for the diaphragm and air are given in Table S2. The pressure difference across the diaphragm is converted into the voltage by the conversion optoelectronics unit. The voltage V_{out}, corresponding to the pressure difference, can then be calculated based on the basic circuit theory for the incident acoustic pressure P_{in} at the angular frequency *w* with the formula as follows,

$$V_{out} \propto \frac{1/\ jwC_{dia}}{1/\left(1/Z_1 + 1/Z_2\right) + 1/\ jwC_{cav}} \frac{Z_2}{Z_1 + Z_2} P_{in} \tag{S1}$$

where Z_1 and Z_2 are the electrical impedances described as,

$$Z_1 = jwM_{rad} + R_{rad} + jwM_{dia} + 1/\ jwC_{dia} \tag{S2}$$

$$Z_2 = jwM_{hole} + R_{hole} \tag{S3}$$

The frequency response of the FPAS can be obtained by multiplying the voltage V_{out} with the acoustic sensitivity of the diaphragm S_d. S_d is defined as the ratio of the deflection of the diaphragm center to the applied acoustic pressure and is a constant dependent on the geometric and mechanical parameters of the diaphragm. Therefore, the relative amplitude of the diaphragm deflection as a function of the acoustic angular frequency is plotted to represent the frequency response of the FPAS. Here, as the effect of residual stress is found to dominate over the flexural rigidity in the thin polymer membrane of the FPAS, the lumped parameters corresponding to the membrane model instead of the plate model are used in Table S1. Fig. S4 shows the calculated frequency response of the FPAS with membranes of different hole sizes in the frequency range from 0.1 kHz to 1 MHz. Considering the irregular shape of the holes, an equivalent hole radius which corresponds to a circular hole with an equal area is used to define the hole size.

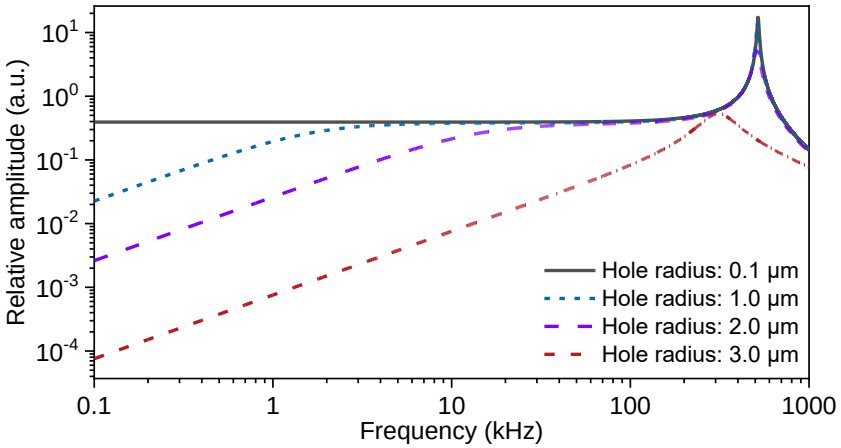

Fig. S4. Frequency response of the FPAS to acoustic waves in the range of 0.1 kHz to 1MHz as calculated by the equivalent circuit model for the membrane with equivalent hole radii of 0.1 μm, 1 μm, 2 μm and 3 μm.

Table S1. Parameters for the lumped elements in the equivalent circuit for FPAS.

Description	Symbol	Expression
Radiation mass of diaphragm	M_{rad}	$\frac{8\rho_{air}}{3\pi^2 r_{dia}}$
Radiation resistance of diaphragm	R_{rad}	$\frac{\rho_{air} w^2}{2\pi c}$
Acoustic mass of diaphragm	M_{dia}	$\frac{4\rho_{dia} h_{dia}}{3\pi r_{dia}^2}$
Compliance of diaphragm	C_{dia}	$\frac{\pi r_{dia}^4}{8 h_{dia}\sigma}$
Resistance of holes from vertical flow	R_{holeV}	$R_{holeH} = \frac{6\mu\left(\xi - \frac{1}{4}\xi^2 - \frac{1}{2}\ln\xi - \frac{3}{4}\right)}{\pi L^3}$
Resistance of holes from horizontal flow	R_{holeH}	$R_{holeV} = \frac{8\mu h'}{\pi r_{hole}^4}$
Resistance of holes	R_{hole}	$\frac{R_{holeV} + R_{holeH}}{N}$
Effective thickness 1	h'	$h' = h_{hole} + \frac{3\pi}{8} r_{hole}$
Radiation mass of holes	M_{hole}	$M_{hole} = \frac{4\rho_0 h''}{3\pi r_{hole}^2}$
Effective thickness 2	h''	$h'' = h_{hole} + \frac{2}{\pi} r_{hole}$
Cavity compliance	C_{cav}	$\frac{\pi r_{dia}^2 L}{\rho c^2}$

Table S2. Physical constants used for the lumped elements in the equivalent circuit.

Description	Symbol	Value	Description	Symbol	Value
Diaphragm radius	r_{dia}	37.5 μm	Young's modulus	E_{dia}	0.138 GPa
Diaphragm thickness	h_{dia}	0.2 μm	Poisson's ratio	v	0.26
Diaphragm density*	ρ_{dia}	998 kg/m^3	Density of air	ρ_{air}	1.21 kg/m^3 (20 ℃)
Stress in diaphragm	σ	1.2 MPa	Sound speed in air	c	343 m/s
Cavity length	L	60 μm	Dynamic viscosity	μ_{air}	1.82×10^{-5} kg/m/s
Equivalent hole radius	r_{hole}	1 μm	Air filling factor	ξ	$N\cdot(r_{hole}/r_{dia})^2$
Hole thickness	h_{hole}	0.2 μm	Hole number	N	*4*

*The density of the diaphragm made from UV curing adhesive is assumed to be equal to the water.

Supplementary Note 3. Spectral stability of FPAS

The temporal evolutions of the reflection spectra for the FPASs with the intact and the patterned membranes are recorded for a duration of ~ 3 hours. The patterned membrane has holes of an equivalent radius of 2 μm. The corresponding spectral wavelength shifts of the FPASs are compared in Fig. S5. In the laboratory condition, the spectral wavelength shift of the FPAS reduces from ~ 5 nm to less than ~ 0.1 nm after patterning the holes in the membrane. This spectral drift is ~ 2% of the linear working range (~ 5 nm) for the FPAS (see Fig. S1(c)), which is supposed to induce negligible fluctuations to the detected acoustic signals. This is a result of the laser-patterned membrane holes that actually act as a high-pass filter, greatly reducing the low-frequency environmental air flow and pressure disturbances compared with the FPAS with an intact membrane.

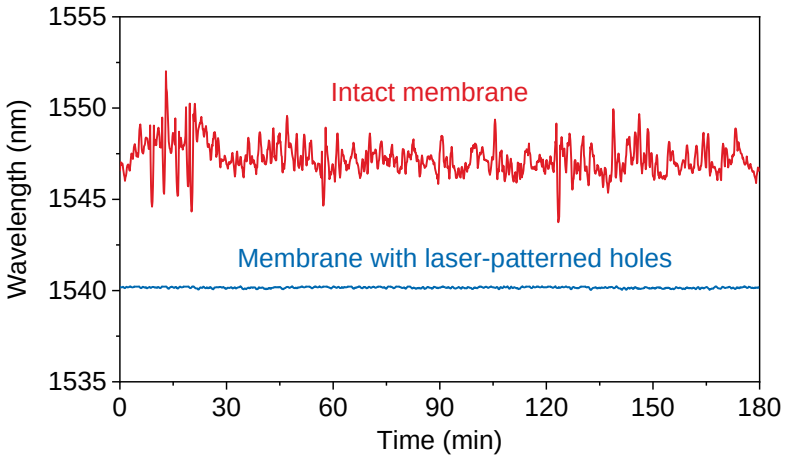

Fig. S5. Spectral stability of the FPAS before and after patterning holes in the membrane. The equivalent hole radius is ~ 2 μm.

Supplementary Note 4. Factors affecting the acoustic sensitivity of FPAS

The acoustic sensitivity of the FPAS with different membrane thickness is evaluated by characterizing the noise-equivalent pressure (NEP). As shown in Fig. S6, the FPAS with a submicron-thick (~ 200 nm) membrane exhibits a ~ 15 dB lower noise-equivalent pressure (NEP) compared with the FPAS with a thickness of ~ 3.8 μm. The thinner membrane provides a higher acoustic sensitivity, which agrees with the trend predicted by the formula describing the pressure induced deflection of a thin elastic membrane [33]. Currently, the thinnest membrane prepared in the fabrication process is ~ 200 nm. Further reduction of the membrane thickness is found to increase the possibility of forming small pores in the membrane. Another aspect needs to be mentioned is the pre-stress formed in the membrane during the photothermal actuation process. The membrane is pressurized by the isotropic pressure difference across the pre-cured membrane after the switching off the 980 nm heating light (see Fig. S1). The pre-stress in the membrane after fully curing keeps the membrane taut on the cavity without wrinkles, which is critical for an elastic thin membrane to sensitively response to external acoustic waves.

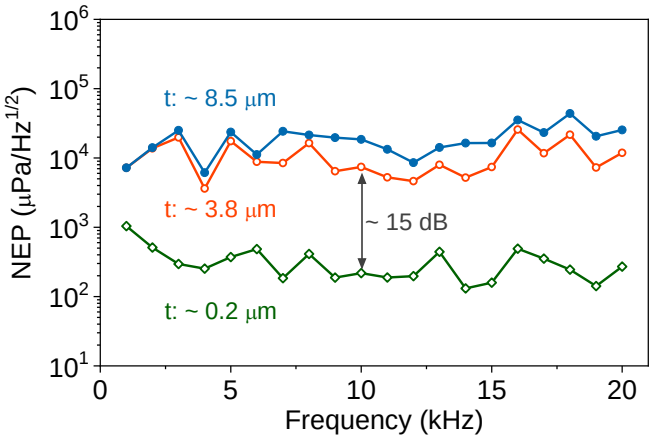

Fig. S6. NEP of the FPAS with different membrane thickness to acoustic waves in the frequency range of 1 kHz to 20 kHz.

Supplementary Note 5. Acoustic sensitivity for FPAS with different cavity diameters

The acoustic responses of the FPASs with different cavity diameters are measured in the frequency range from 1 kHz to 20 kHz as shown in Fig. S7. The sensitivity is obtained by dividing the output voltage from the photodetector by the acoustic pressure measured by the calibration microphone. The fabrication process of the FPAS with a cavity diameter of 25 μm is the same with that for a cavity diameter of 75 μm. For the FPAS with a cavity diameter of 150 μm, a capillary with an outer diameter of 330 μm and a bore diameter of 150 μm that is larger than the diameter of the SMF is used. The SMF is firstly inserted into the capillary monitored under the microscope. Once the distance between the fiber tip end and the opening of the capillary reaches the designated value, UV curing adhesive is applied to the gap between the fiber and the capillary from the other opening of the capillary and cured by the UV lamp. The fabrication of the suspended membrane covering the cavity follows the same procedure as that for the FPAS with a 75 μm-diameter cavity. For each cavity diameter, three samples are prepared and tested. The acoustic sensitivity of the FPAS with a cavity diameter of 150 μm is ~ 4 times of that for the FPAS with a cavity diameter of 75 μm. This result is close to the theory predication, which suggests that the acoustic sensitivity of the FPAS with a thin membrane is proportional to the square of its diameter. The acoustic sensitivity of the FPAS with a cavity diameter of 75 μm is ~ 16 times of that for a cavity diameter of 25 μm. This value is larger than the theoretically predicted value of 9 times, and might be caused by the biconcave shape of the membrane. For the cavity with a small diameter, the increase in the effective membrane thickness due to the slightly larger thickness of the membrane near the capillary edge than that at the membrane center becomes non-negligible and thus reduces the acoustic sensitivity.

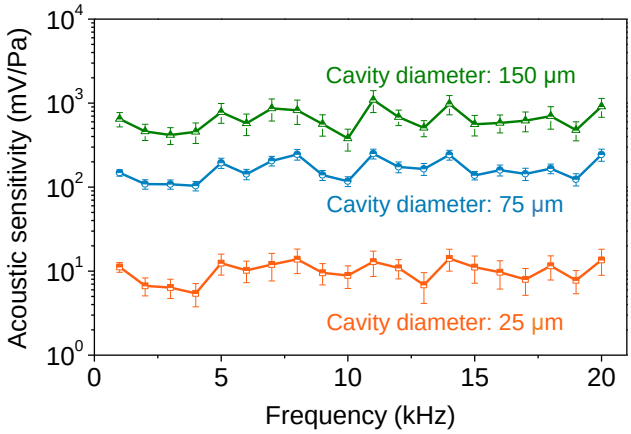

Fig. S7. Acoustic sensitivity of the FPAS with different cavity diameters to acoustic waves in the frequency range from 1 kHz to 20 kHz.

Supplementary Note 6. Theoretical analysis of the localized photoacoustic wave field

To obtain a more intuitive picture of the spatial distribution of the localized PA wave field, the locally-generated PA wave in the F-P cavity is modelled in the frequency domain using the thermoviscous acoustics interface in the pressure acoustics module of the finite element analysis software (Comsol 6.0). To figure out the dependence of the PA wave amplitude on the cavity diameter, a simplified model of two end-closed silica capillary is studied and the simulated results are plotted in Fig. S8.

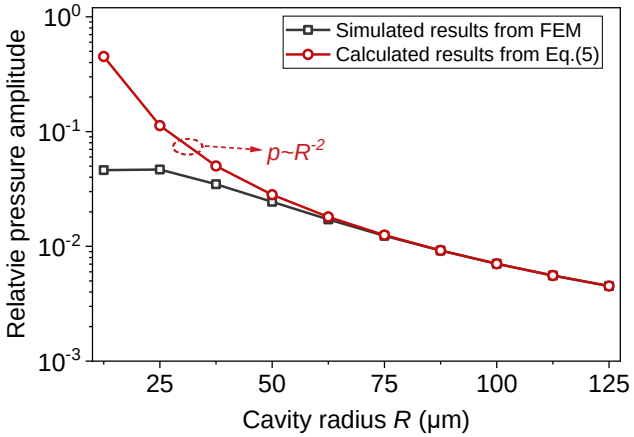

Fig. S8. Acoustic pressure amplitude inside the cavity with different radii obtained from the simulation and the calculation based on Eq. (5). The cavity has a length of 60 μm and the acoustic wave frequency is 7 kHz in the simulation and calculation.

As the acoustic wavelength is much larger than the cavity radius, the pressure field is uniformly distributed inside the cavity and increases with the reduction in the cavity radius. This trend agrees well with the results calculated using Eq. (5), where the acoustic pressure p scales with the cavity radius following the relationship $p \sim R^{-2}$. As the cavity radius reduces to be smaller than 50 μm, the simulated results gradually deviate from the calculated values, due to the loss caused by the viscous and thermal effects. The viscous boundary layer thickness $\delta_v=(2\mu_{air}/w\rho_{air})^{1/2}$ and the thermal boundary layer thickness $\delta_t=(2K/w\rho_{air}C_P)^{1/2}$, where K is the gas thermal conductivity and C_p is the heat capacity at constant pressure. In air at 20 ℃ and 1 atm, the thickness of the viscous boundary layer and the thermal boundary layer are ~ 0.026 mm and ~ 0.031 mm at 7 kHz, respectively. The acoustic loss induced by these effects reduces the PA response of the FPAS with a small cavity radius.

Based on the analytical expression (Eqs. (5-6)) for describing the photoacoustic (PA) waves locally-generated in the F-P cavity of the FPAS, the relationship between the amplitude of the PA wave and the modulation frequency of the pump laser is calculated and plotted in Fig. S9. The amplitude of the PA wave in the low frequency region below 10 kHz is high-pass filtered due to the damping caused by the gas and heat flows through the membrane holes. In comparison, the PA wave in the high-frequency region is low-pass filtered by the thermal damping caused by gas molecules [36].

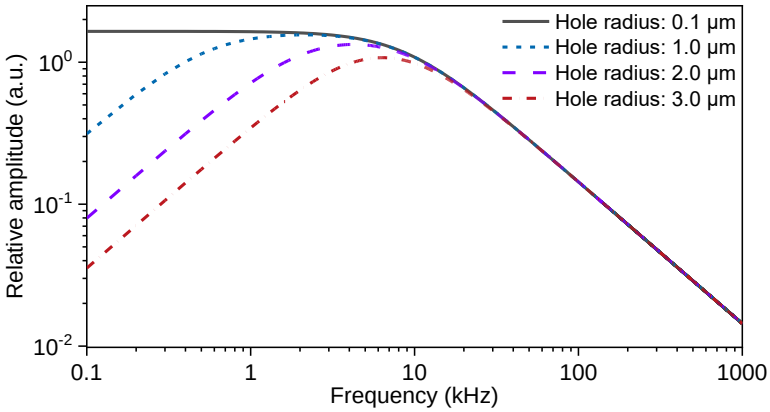

Fig. S9. Relative amplitude of the localized PA wave in the F-P cavity of the FPAS as a function of the frequency for membranes with equivalent hole radii of 0.1 μm, 1 μm, 2 μm and 3 μm.

By combining the acoustic response as calculated based on Eq. (S1-S3), the PA response of the FPAS in the frequency domain can be obtained as given in Fig. S10(a). Ideally, working at the resonant frequency is preferred to achieve high sensitivity. However, it is found that the measured mechanical resonance of the membrane (See Fig. S10(b)) is actually damped more severely than the predication, since the non-radiative relaxation effect of C_2H_2 gas molecules accounting for the relaxation time from the light absorption to the heat generation is neglected in the theoretical model. The shift in the resonant frequency after the hole pattering may be attributed to the stress induced during the fs-laser inscription of the membrane.

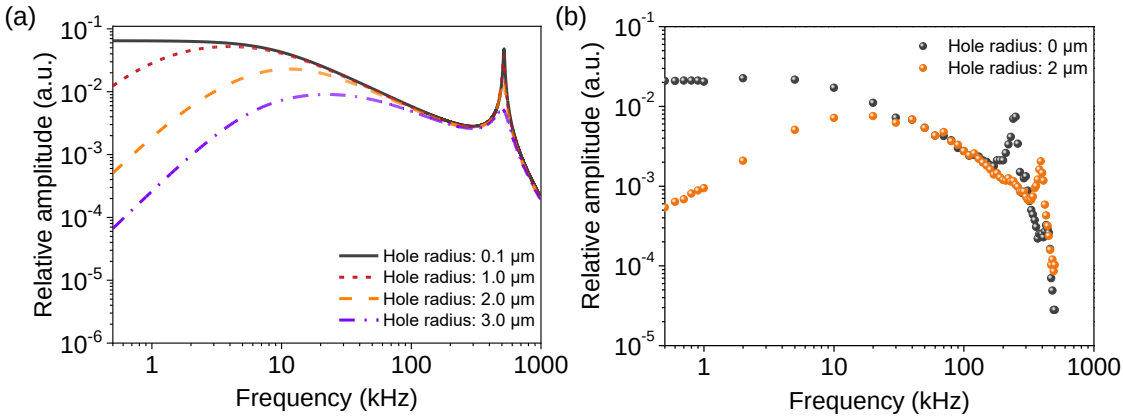

Fig. S10. Relative amplitude of localized PA wave in the F-P cavity of the FPAS as a function of the frequency for membranes with different hole sizes. (a) Calculated results for membranes with the equivalent hole radii of 0.1 μm, 1 μm, 2 μm and 3 μm. (b) Measured results for membranes with the equivalent hole radii of 0 μm and 2 μm.

Next, as shown in Fig. S11(a), the interaction of the membrane with the PA waves is modelled by the shell interface in the solid mechanics module of software Comsol 6.0 in the frequency domain. To avoid acoustic reflection at the boundary of the simulation domain, a perfectly matched layer (PML) in the pressure acoustics module is added. Acoustics-thermoviscous acoustics boundary is set to the interface between the domains of the surrounding air and the PML for multi-physics coupling. Thermoviscous acoustics-structure boundary is set to the interface between the domains of the air surrounding the cavity and membrane. A Gaussian beam with the waist diameter of ~ 10 μm, equal to the mode field diameter of the SMF, is used as the domain feature of heat source for the PA signal generation. The membrane is approximated by a homogeneous polymer layer with a uniform thickness of 200 nm. The pre-stress in the stretched membrane (~ 1.2 MPa) is included as the initial stress in the simulation. The silica capillary wall and the bottom of the F-P cavity is modelled as hard boundary walls, as a result of the large acoustic impedance compared with the air. The

membrane is modelled as free surface with fixed edges along the cavity inner periphery. To be less computationally intensive, a quarter of the full spherical domain is simulated by applying the symmetric condition. The radius of the quarter-spherical acoustical domain is 300 µm and the PML has a thickness of 60 µm. The element size of the finite element mesh is one half of the viscous boundary layer thickness in the air for the thermoviscous domain and one fifth of the acoustic wavelength in the acoustic domain. The geometrical and physical parameters used in the simulation can be found in Table S2. Figure S11(b) shows the PA responses of the FPASs with membranes of different hole radii in the frequency range from 1 kHz to 1 MHz, featuring a similar trend with the measured results in Fig. S10(b).

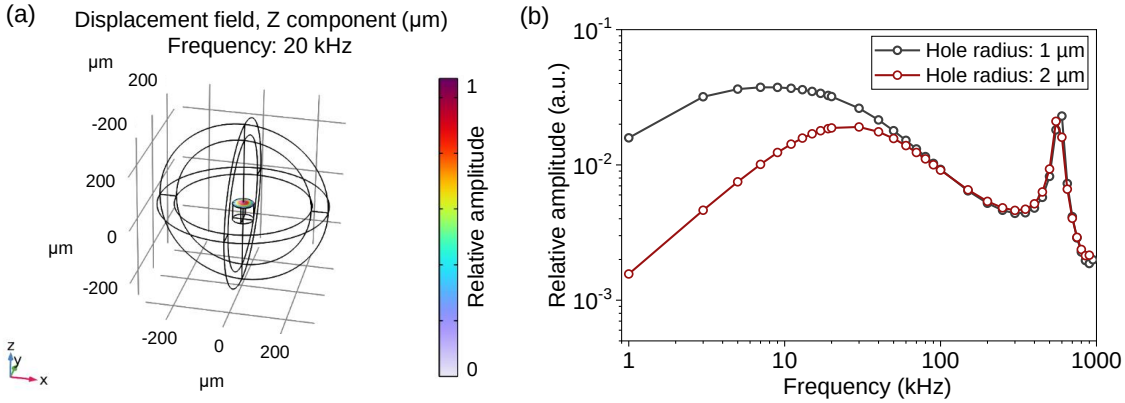

Fig. S11. (a) Three-dimensional (3-D) finite element model for simulating the interaction between the membrane and the locally-generated PA wave in the frequency domain. (b) Calculated PA response of the FPAS with membranes of the equivalent hole radii of 1 µm and 2 µm in the frequency range from 1 kHz to 1 MHz.

Supplementary Note 7. Allan deviation analysis

To evaluate the long-term stability and the detection limit of the FPAS, the pump laser wavelength is tuned away from the absorption line of the gas molecules and the peak value of the output 2f signal from the FPAS is subsequently recorded over a duration of 120 minutes continuously. Allan deviation of the recorded signals is calculated and plotted in Fig. S12, which shows a good agreement with $t^{-1/2}$ fitting, indicating that the FPAS performance is dominated by the white noise. The noise is estimated to be ~ 0.17 μV for an average time of ~ 200 s, corresponding to a detection limit of ~ 9 ppb for C_2H_2 gas since the peak-to-peak (pk-pk) value of the 2f signal from the FPAS is ~ 4.82 mV for a gas concentration of 250 ppm.

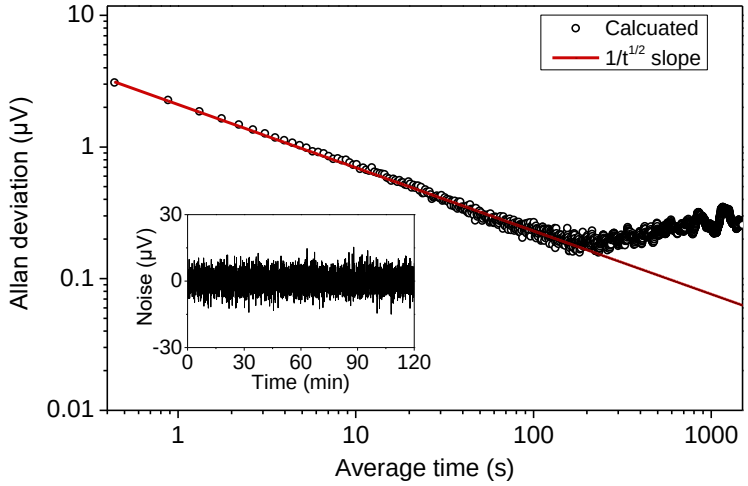

Fig. S12. Allan deviation plot for the FPAS. Inset: recorded signals over a duration of 120 minutes.

Supplementary Note 8. Dynamical range and response time of the FPAS

The dynamic range of the FPAS is characterized by measuring the output 2f signal to the C_2H_2 gas concentration ranging from 0.1% to 30%. As the gas concentration increases to 5%, the FPAS starts to response nonlinearly, which can be observed from the pk-pk values of the 2f signals in the range from 5% to 30%, as indicated by the red ellipse in Fig. S13(a). The corresponding 2f signals recorded at various gas concentrations are also given, as plotted in Fig. S13(b).

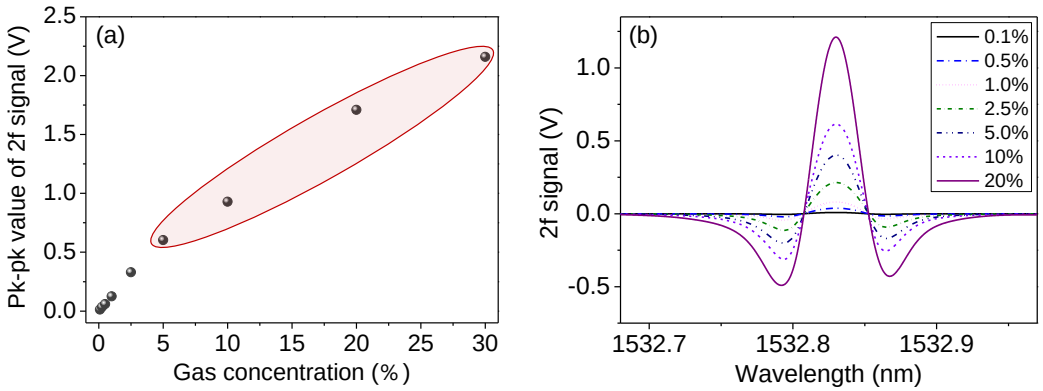

Fig. S13. (a) Pk-pk values of the 2f signals from the FPAS for the gas concentration ranging from 0.1% to 30%. (b) 2f signals at different gas concentrations.

Supplementary Note 9. Response time

The response time of the FPAS is determined by the diffusion time of the gas into the cavity. To study the dynamics of the gas diffusion governed by the Fick's law, a 3-D model for the FPAS cavity covered by the membrane is studied with the interface (transport of diluted species) under the chemical species transport branch in the software Comsol 6.0. The time-dependent molar concentrations of the C_2H_2 gas at the bottom of the cavity for the membranes with different hole sizes are shown in Fig. S14. The cavity length and the cavity inner diameter in the simulation are 60 μm and 75 μm, respectively. The diffusion coefficient for the C_2H_2 molecules in the air is ~ 1.78×10^{-6} m^2/s [65]. The diffusion time reduces as the hole size increases due to the large influx area of the gas. For the equivalent hole radii of 0.5 μm and 1 μm, the diffusion time for the gas concentration from 10% to 90% is ~ 1.8 ms and ~ 1.1 ms, respectively. For the equivalent hole radius of 1 μm, by increasing the cavity length to 600 μm, the diffusion time increases to 22 ms. Therefore, the short response time of the FPAS is a result of the microscale cavity length.

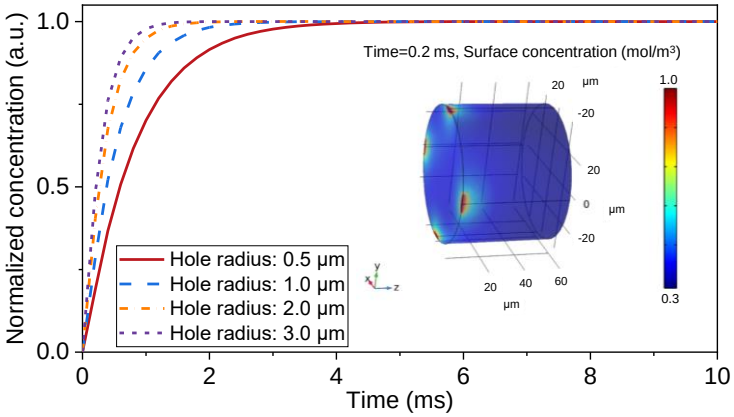

Fig. S14. Calculated time-dependent molar concentration of the C_2H_2 gas in the cavity for the membrane with different equivalent hole radii. Inset: simulated molar concentration field at the time of 0.2 ms for an equivalent hole radius of 1 μm.

Supplementary Note 10. Dissolved carbon dioxide (CO_2) measurement with middle-infrared laser

The configuration of the 2006 nm fiber laser source is illustrated in Fig. S15(a). A laser diode (Eblana Photonics, EP2004-DM-B) operation at ~ 2006 nm is used as the seed and amplified by 5 m-long thulium-doped fiber. After passing through the fiber isolator, the 2006 nm laser light is combined with the pump light at 793 nm by the bundle combiner. The optical filter is used to filter off the residual pump light. The maximum power of the amplified 2006 nm laser light under a pump power of 8 W is ~ 200 mW, limited by the coupling loss between the splicing joint of the normal single mode fiber and the thulium-doped fiber. To avoid the possible thermal damage to the fiber joint considering the high pump power, the two sides nearby the fiber joint is attached to a heat sink using the thermal conductive silicone. As the absorption of the CO_2 gas molecules nearby 2006 nm is ~ two orders of magnitude lager than that at 1578 nm (Fig. S15(b)), a NEC of ~ 40 ppm for the CO_2 gas at an integration time of 100 ms can be achieved by using a low laser power of ~ 20 mW, with the measured 2f signal and the noise floor shown in Fig. S15(c).

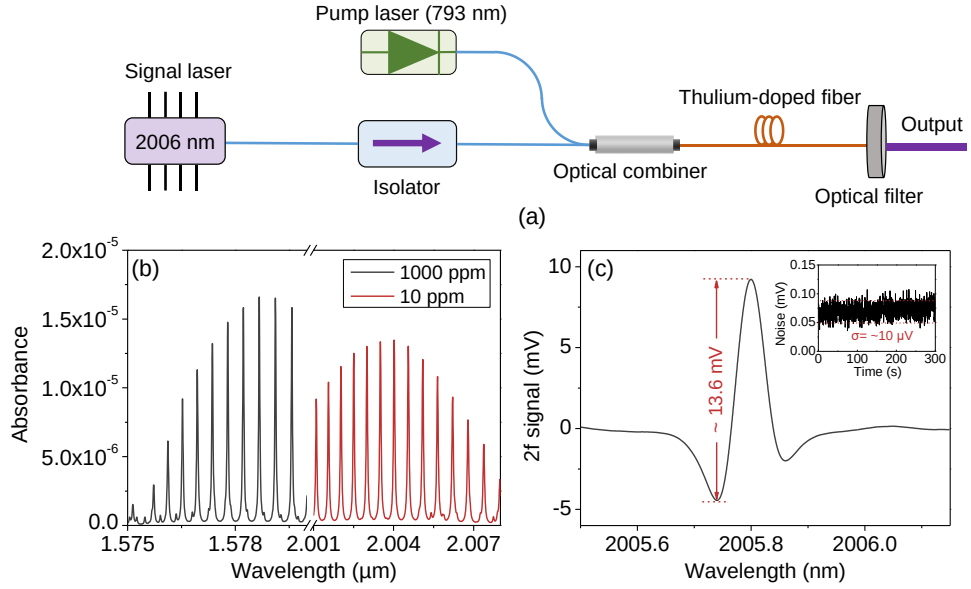

Fig. S15. (a) Configuration of the 2006 nm fiber laser source. (b) Absorption lines of the CO_2 gas nearby the 1578 nm and 2006 nm. (c) 2f signal for the CO_2 gas with a concentration of 5%. Inset: the noise floor.

Supplementary Note 11. Intravascular blood gas monitoring

Fig. S16(a) shows the photograph of the blood gas analyzer for measuring the dissolved CO_2 concentration in the blood sample from the rat tail. The blood sample is drawn into the test card (Fig. S16(b)), which is then inserted into the analyzer card slot. For the in vivo animal experiment, the rat in anesthesia is placed into a home-made plastic chamber, with one end drilled with a hole to pass through the rat tail, as shown in Fig. S16(c). The other end is sealed by a foam with the central hole inserted with a gas tube to inject the gas mixture of oxygen (O_2) and nitrogen (N_2) or CO_2 and air. A 21G syringe needle is pierced into the rat vein as the guiding channel for the following insertion of the FPAS as shown in the inset of Fig. S16(d). Once the FPAS reaches the desired position, the optical fiber pigtail is fixed on the supporting plate.

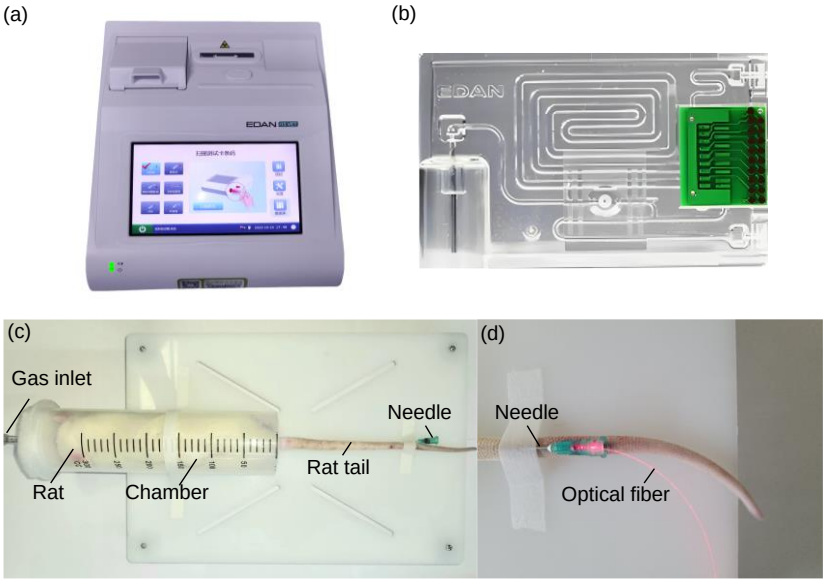

Fig. S16. Photograph of (a) the blood gas analyzer and (b) the test card. (c) Photograph of the experiment apparatus for intravascular blood gas monitoring of the rat in vivo. (d) Close-up photograph of the needle with the inserted FPAS.

Supplementary Note 12. Gas sensing performance comparison

Table S3 Comparison of the vapor/gas sensing performance of different techniques.

Technique	Target analytes	SERS substrate	Detection limit	Response time	Footprint size
SERS	Benzaldehyde[66]	Porous Au+MOF	0.32 ppb	~ 100 s	NA
	Toluene[67]	Porous ZnO coated gold nanoarray	10 ppb	< 30 s	Si wafer (2×2 cm^2)
	DMMP[12]	Mesoporous silica+Au nanoparticle arrays	100 ppb	150 s	Si/SiO_2 wafer (0.4×0.8 cm^2)
	NH_3[68]	Silver-coated silicon nanopillars	<1 ppm	1 s	Glass cover slide
	H_2S[69]	PbO nanosheets+Au film	1 ppb	10 s	Silicon wafer (3×3 mm^2)
	NO_2[70]	Pure gold nanostructures	<50 ppm	NA	Quartz substrate
SEIRAS	CO_2[71]	ZIF-8+Au antenna	80 ppm	< 60 s	Silicon wafer (0.1×0.1 mm^2)
	CH_4[71]		230 ppm		
	CO_2[72]	PEI+metamaterial	40 ppm	≈ 2 min	Silicon wafer (20×20 μm^2)
Middle-infrared waveguide	CO_2[73]	hBN+PEI ribbon arrays	390 ppm	< 2 min	CaF_2 substrate (30×30 μm^2)
	C_2H_2[53]	Ta_2O_5+Al_2O_3 waveguide	7 ppm (T_a= 1 s)	NA	2 cm long
	CH_4[54]	Silicon slot waveguide	0.3 ppm (T_a=50 s)	NA	1.15 cm long
FPAS	C_2H_2[This work]	Polymer membrane on silica fiber tip	9 ppb (T_a=200 s)	20 ms	125 μm in diameter
	CO_2[This work]		40 ppm (T_a=0.1 s)		

SERS: surface enhanced Raman spectroscopy; **SEIRAS**: surface-enhanced infrared absorption spectroscopy; **FPAS**: fiber photoacoustic spectroscopy; DMMP: dimethyl methylphosphonate; MOF: metal-organic framework; ZIF-8: zeolitic imidazolate framework. PEI: polyethylenimine; hBN: hexagonal boron nitride; T_a: average time.